Hystereses in flow-induced compression of a poroelastic hydrogel

Zelai Xu¹, Pengtao Yue², and James J. Feng^{1,3}

¹Department of Chemical and Biological Engineering, University of British Columbia, Vancouver, BC V6T 1Z3, Canada ³Department of Mathematics, Virginia Tech, Blacksburg, VA 24061, USA ³Department of Mathematics, University of British Columbia, Vancouver, BC V6T 1Z2, Canada

July 21, 2024

Abstract

We investigate theoretically the one-dimensional compression of a hydrogel layer by a uniform fluid flow normal to the gel surface. The flow is driven by a pressure drop across the gel layer, which is modeled as a poroelastic medium. The novelty comes from considering, for the first time, the impact of interfacial permeability and compression. This leads to several new features for the flow and gel compression. As the pressure simultaneously drives the Darcy flow through the pores and compresses the gel, the flux-pressure relationship may become non-monotonic. Most interestingly, we discover two types of hysteresis when the pressure or the flux is controlled, which are also confirmed by transient numerical simulations. The first type of hysteresis stems from the interplay between the gel compression at the upstream interface and that in the bulk of the gel, and would not be predicted by models that ignore the interfacial compression. The second type hinges on strainhardening in the gel that maintains a non-vanishing permeability at high pressure. Finally, we suggest experimental setups and conditions to seek such hystereses in real gels.

1 Introduction

Hydrogels are cross-linked polymer networks swollen by a large amount of absorbed water. Being soft, porous and biocompatible, hydrogels have found applications in a wide range of new technologies, including soft sensors and actuators [1,2], drug delivery [3] and tissue engineering [4]. For example, hydrogels are widely used to mimic the extracellular matrix in organ-on-chip devices [5]. In response to ambient changes, hydrogels spontaneously swell or deform, and can thus serve as automatic flow control in microfluidic devices [6]. As soft porous media, hydrogels also exhibit interesting solid and fluid mechanical behavior, which is often denoted by the term poroelasticity [7–9]. In particular, the coupling between fluid flow and solid deformation can give rise to novel phenomena [10,11]. This paper reports one such phenomenon predicted by a poroelastic model.

Consider the one-dimensional (1D) compression of a layer of hydrogel by a normal flow of the solvent (Fig. 1). This flow, in the x direction, is driven by a prescribed

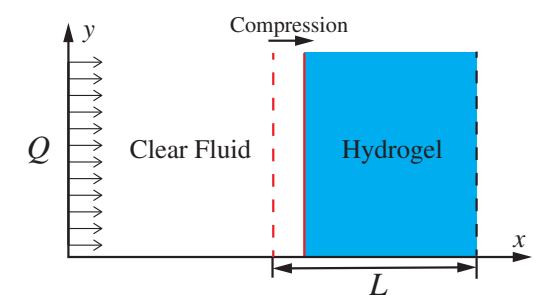


Figure 1: Schematic of 1D compression of a hydrogel layer. The dashed red line marks the initial interface between the clear fluid and the hydrogel, the uncompressed thickness of the hydrogel layer being L. The solid red line marks the displaced interface under compression. The downstream surface of the gel layer is constrained by a fixed permeable mesh (the black dashed line), and has zero displacement. The uniform velocity of the clear fluid Q is driven by a pressure drop P between the fluid upstream and downstream of the gel layer.

pressure drop across the layer. The gel layer extends to infinity in the y and z directions, with zero displacement in these transverse directions. The downstream surface of the gel layer is fixed in space but allows passage of the solvent, as if by a stiff mesh. The upstream gel surface is displaced by the flow as the layer compacts.

For a rigid porous medium, Darcy's law posits a fluid flux Q that is linearly proportional to the imposed pressure drop P. For a soft porous material such as a hydrogel, however, the pressure and Darcy drag compact the solid network and reduce the pore space. Thus, the flux becomes a nonlinear function of the imposed pressure, falling below the linear prediction of Darcy's law at a pressure on the order of the bulk modulus of the hydrogel [12]. Since the compaction problem embodies a key feature of poroelasticity, it has been studied by several groups in the past, e.g., [10, 11, 13–25]. Some used the problem as a test of their poroelastic models [11, 19], while others investigated compaction of deformable porous media, hydrogels or biological tissues in engineering and biological applications [14, 15, 21–23, 25].

We will tackle the compression problem with a poroelastic model that differs from most of the above in the entry boundary condition (EBC) at the upstream interface between the gel layer and the clear fluid. Prior poroelastic models assumed a continuity of normal stress or pressure at gel-solvent boundaries, following a long tradition of such treatment for rigid porous media [26-30]. Based on physical intuition of a contraction flow into the pores, however, we anticipate a finite pressure drop across the fluid-gel interface. This idea was developed into pressure-jump interfacial conditions for rigid porous media via a homogenization procedure [31, 32]. More recently, Lācis et al. [33] proposed a transpiration-resistance model for the interfacial pressure jump, and demonstrated interesting physics in a lid-driven flow above a rigid porous medium. For poroelastic media, we have pursued a similar idea by formulating the interfacial dissipation in the context of irreversible thermodynamics. Thus, the constraint of a positive entropy production leads to an EBC that posits a linear proportionality between the velocity jump and the traction jump across the interface [34,35]. Subsequently, Xu et al. [24] have established the superiority of the newly proposed EBC to those in the porous media literature, and validated it against experimental data in shear flows. Naturally, one wonders if the new EBC would bring new physics into the gel-compression

This paper presents the theoretical predictions of our model for the 1D compression

of a hydrogel layer. First, we describe how our model predicts two types of hystereses in certain parameter regimes, with either the pressure P or the flux Q being controlled. Second, we examine the roles of EBC and the bulk permeability in the first type of hysteresis. Finally, we discuss the experimental conditions that may allow the hystereses to be observed in the laboratory.

$\mathbf{2}$ Formulation of poroelastic model

From this point onward, dimensional quantities will carry an overbar, while dimensionless ones do not. The governing equations are essentially the same among various poroelastic models published before [11, 19, 24, 36], barring minor differences in simplifications and notations. We adopt the continuity equations for the fluid and solid phases and their momentum equations in the absence of gravity:

$$\frac{\partial(1-\phi)}{\partial \bar{t}} + \nabla \cdot [(1-\phi)\bar{\mathbf{v}}_f] = 0, \qquad (1)$$

$$\frac{\partial\phi}{\partial \bar{t}} + \nabla \cdot (\phi\bar{\mathbf{v}}_s) = 0, \qquad (2)$$

$$\frac{\bar{\mu}}{\bar{k}}(1-\phi)(\mathbf{v}_f - \mathbf{v}_s) + \nabla \bar{p} = 0, \qquad (3)$$

$$\frac{\partial \phi}{\partial \bar{t}} + \nabla \cdot (\phi \bar{\mathbf{v}}_s) = 0, \tag{2}$$

$$\frac{\bar{\mu}}{\bar{k}}(1-\phi)(\mathbf{v}_f - \mathbf{v}_s) + \nabla \bar{p} = 0, \tag{3}$$

$$\nabla \cdot (\phi \bar{\sigma}_s) - \nabla \bar{p} = 0, \tag{4}$$

where ϕ is the solid volume fraction and $1-\phi$ is the fluid volume fraction, also known as the porosity, and $\bar{\mathbf{v}}_f$ and $\bar{\mathbf{v}}_s$ are the intrinsic phase average velocities of the fluid and solid phases [37]. Summing the first two equations yields an overall continuity equation $\nabla \cdot [(1-\phi)\bar{\mathbf{v}}_f + \phi\bar{\mathbf{v}}_s] = 0$, whose implementation requires the hydrodynamic pressure \bar{p} as a Lagrange multiplier. Equation (3) is Darcy's law for the fluid flow, $\bar{\mu}$ being the fluid viscosity and \bar{k} the permeability. The Brinkman stress term has been neglected as it is typically small compared to the Darcy drag; scaling arguments for this common practice can be found in the literature [26, 38]. Equation (4) is the classical Biot equation that expresses the overall force balance on the poroelastic two-phase mixture. The extra solid stress tensor $\bar{\sigma}_s$ is defined such that $\phi \bar{\sigma}_s$ is Terzaghi's effective stress [11].

For the 1D geometry of the compression problem, the governing equations can be simplified into scalar forms:

$$\frac{\partial(1-\phi)}{\partial \bar{t}} + \frac{\partial[(1-\phi)\bar{v}_f]}{\partial \bar{x}} = 0, \tag{5}$$

$$\frac{\partial \phi}{\partial \bar{t}} + \frac{\partial (\phi \bar{v}_s)}{\partial \bar{x}} = 0 \tag{6}$$

$$\frac{\bar{\mu}}{\bar{k}}(1-\phi)(\bar{v}_f - \bar{v}_s) + \frac{\partial \bar{p}}{\partial \bar{x}} = 0,$$

$$\frac{\partial(\phi\bar{\sigma}_s)}{\partial \bar{x}} - \frac{\partial \bar{p}}{\partial \bar{x}} = 0,$$
(8)

$$\frac{\partial(\phi\sigma_s)}{\partial\bar{x}} - \frac{\partial\bar{p}}{\partial\bar{x}} = 0, \tag{8}$$

where $\bar{\sigma}_s$ is a shorthand for the solid normal stress $\bar{\sigma}_{sxx}$.

Permeability 2.1

In general, the permeability \bar{k} depends on the pore structure of the medium, including pore size, porosity, tortuosity and connectivity. In the porous-media literature, k has been modeled using two different approaches: treating the flow through a porous medium as external flow around an array of solid particles, or as internal flow through myriad conduits. A detailed account of the historical development of both approaches can be found in Dullien [39], who also evaluated their overlap and differences. In particular, the external-flow models are more appropriate for high-porosity media, whereas the internal-flow ones work better for low-porosity media. For our purpose, we will test two widely used formulas representative of the two types:

$$\bar{k}_{\rm D} = \frac{2\bar{r}^2}{9} \frac{1-\phi}{\phi},$$
 (9)

$$\bar{k}_{\rm KC} = \frac{\bar{r}^2}{45} \frac{(1-\phi)^3}{\phi^2},$$
 (10)

where \bar{r} is a characteristic length scale for the pores. The Darcy permeability $\bar{k}_{\rm D}$ arises from the Stokes drag on a dilute array of spheres of radius \bar{r} separated by an average distance \bar{H} such that $(4\pi\bar{r}^3/3)/\bar{H}^3=\phi$. The total drag over a certain volume must balance the imposed pressure drop across that volume. Comparing this balance with Darcy's law gives us Eq. (9), which also agrees with the result of a more formal homogenization procedure [40]. For denser arrays, hydrodynamic interaction among the particles tends to decrease the permeability [41,42], but these formulas reduce to $\bar{k}_{\rm D}$ in the limit of high porosity. The Kozeny-Carman permeability $\bar{k}_{\rm KC}$ is based on modeling the flow in porous media as through tortuous conduits [11,39], with \bar{r} representing the characteristic pore radius. Our continuum model, of course, does not specify the length scale \bar{r} directly, and we will treat the characteristic permeability $\bar{k}^* = 2\bar{r}^2/9$ as a material property of the hydrogel.

As hydrogels typically have low solid content and high porosity ($\phi \sim 0.02$, and can be as low as 0.003) [10, 43–45], $\bar{k}_{\rm D}$ should be more suitable than $\bar{k}_{\rm KC}$ in our context. In particular, $\bar{k}_{\rm D}$ captures the correct high-porosity scaling $\bar{k}_{\rm D} \propto \phi^{-1}$ [39], whereas $\bar{k}_{\rm KC} \propto \phi^{-2}$ as $\phi \to 0$. Thus, we will adopt $\bar{k}_{\rm D}$ in our model, except when making explicit comparisons with $\bar{k}_{\rm KC}$.

2.2 Stress-strain relation

We have used linearly elastic and hyperelastic constitutive equations in the past, mostly for problems with small to moderate strains [24, 25, 36]. The 1D compression problem incurs large strains, however, and we must consider the limit at which most of the pore spaces have been eliminated by the deformation of the solid network. Barring compressibility or failure of the solid material, no further deformation is possible, and the solid stress diverges at this maximum strain e_m . The magnitude of e_m may depend on the shape and size distribution of the pores or solid grains, as well as on the packing configuration.

For hydrogels, such strain-hardening behavior has been studied in shear [46] and uniaxial stretching or compression [47,48], but not in 1D compression. To capture the qualitative feature, we adopt the following constitutive relation for the 1D compression of a porous medium [19,49]:

$$\bar{\sigma}_s = \frac{\bar{E}}{\phi} \frac{e}{1 - \frac{e}{e_m}},\tag{11}$$

with \bar{E} being an elastic modulus and e being the engineering or nominal strain. In general, \bar{E} depends on the polymer concentration and molecular conformation, including chain entanglement and crosslinking. For the flow-induced compression, none of these factors change and we take \bar{E} to be a constant. Compressive strain and stress are negative by convention. In 1D compression, e is related to the local solid fraction by $e = (\phi_0 - \phi)/\phi$, ϕ_0 being the uniform solid fraction in the undeformed hydrogel [11,19,36].

Thus, the maximum strain corresponds to a maximum solid fraction $\phi_m = \phi_0/(1 + e_m)$. Now the constitutive equation can be rewritten as:

$$\bar{\sigma}_s = -\frac{\bar{E}}{\phi} \frac{\phi_m - \phi_0}{\phi_0} \frac{\phi - \phi_0}{\phi_m - \phi}.$$
 (12)

2.3 Boundary conditions

Previous models have almost always assumed pressure continuity on the interface [26–30], which implies zero resistance to the fluid entering small pores, and consequently zero compression of the solid network at the upstream boundary [19]:

$$\bar{\sigma}_s = 0. \tag{13}$$

Intuitively, however, one visualizes the flow entering pores as a contraction flow with its attendant pressure drop and viscous dissipation. This should amount to an entry resistance.

This idea has been formulated via a procedure of irreversible thermodynamics to derive EBCs that ensure positive interfacial entropy production [24, 34, 35]. Thus we arrive at an EBC that stipulates a proportionality between the jump in normal velocity across the fluid-gel interface and the jump in normal stress:

$$\bar{Q} - \bar{v}_f = \bar{\eta}(\bar{\sigma}_s + \bar{P}_E),\tag{14}$$

where the positive coefficient $\bar{\eta}$ can be called an interfacial permeability [34], analogous to the Darcy permeability \bar{k} , and $\bar{P}_E > 0$ is the entry pressure drop across the upstream surface of the gel layer. This EBC implies that the normal stress imbalance between the outer fluid and the solid skeleton injects the solvent into the gel, with $1/\bar{\eta}$ being effectively an interfacial resistance to the injection. Two additional boundary conditions are the continuity of the fluid flow: $\bar{Q} = (1-\phi)\bar{v}_f + \phi\bar{v}_s$, and normal force balance: $\bar{P}_E = -\phi\bar{\sigma}_s$. The latter represents the pressure drop across the entry boundary being sustained by Terzaghi's effective stress in the solid network, the Brinkman stress for the pore fluid having been neglected. Using these, our EBC can be rewritten as

$$\bar{P}_E = -\phi \bar{\sigma}_s = \frac{\phi^2}{(1-\phi)^2} \frac{\bar{Q} - \bar{v}_s}{\bar{\eta}} = \frac{\bar{\mu}}{\tilde{\eta}} (\bar{Q} - \bar{v}_s), \tag{15}$$

where $\tilde{\eta} = \bar{\mu}\bar{\eta}(1-\phi)^2/\phi^2$ is a penetration length [50,51]. It absorbs the solvent viscosity μ in anticipation of $\bar{P}_E \propto \bar{\mu}$, and is thus a geometric quantity comparable to the Navier slip length. Obviously, the stress-free EBC of Eq. (13) can be recovered from Eq. (15) in the limit of $\tilde{\eta} \to \infty$. In general, $\tilde{\eta}$ is a function of the pore size \bar{r} and the solid fraction ϕ , and scaling dictates $\tilde{\eta} = \psi(\phi)\bar{r}$, with a dimensionless function $\psi(\phi)$. Using porescale models for the gel surface, Xu et al. [51] have recently studied $\psi(\phi)$ by numerical computation and scaling arguments, and recommended the following semi-analytical expression that adequately represents the numerical data:

$$\tilde{\eta} = \frac{(1-\phi)^2}{1+\phi^2}\bar{r},\tag{16}$$

which will be used in this study. This formula implies that $\tilde{\eta}$ is on the order of \bar{r} . Thus, interfacial penetration is governed by the same pore size as determines the bulk permeability \bar{k}^* . Besides, $\tilde{\eta}$ decreases with increasing solid fraction ϕ , signifying increasing resistance to penetration. The new EBC of Eq. (15) is key to the predictions of our model, as will be illustrated in Section 3. In steady state, we set $\bar{v}_s = 0$ in Eq. (15).

At the downstream boundary (Fig. 1), the solid network is fixed: $\bar{\mathbf{v}}_s = 0$, and the pressure is set to zero: $\bar{p} = 0$. As the problem is one-dimensional, there is no transverse flow or displacement along the y direction.

2.4Scaling

The following scalings are used to render the governing equations and boundary conditions dimensionless:

$$x = \bar{x}/\bar{L}, \quad (v_s, v_f) = (\bar{v}_s, \bar{v}_f)/\bar{V}, \quad (\sigma_s, p) = (\bar{\sigma}_s, \bar{p})/\bar{E}, \tag{17}$$

where \bar{L} is the undeformed thickness of the gel layer, and $\bar{V} = \bar{E}\bar{k}^*/(\bar{L}\bar{\mu})$ is the characteristic velocity, with the characteristic permeability $\bar{k}^* = 2\bar{r}^2/9$. Naturally, \bar{L}/\bar{V} serves as the time scale. Thus, the problem is governed by four dimensionless parameters:

$$\eta = \bar{r}\bar{L}/\bar{k}^*, \quad P = \bar{P}/\bar{E}, \quad \phi_m, \quad \phi_0. \tag{18}$$

The penetration length $\tilde{\eta} \propto \bar{r}$ is scaled by $\bar{k^*}/\bar{L}$ into η , which carries the physical meaning of the ratio between the interfacial and bulk permeability. It also represents the number of pores in the gel thickness: $\eta = 4.5 L/\bar{r}$, and is related to the Darcy number $Da = \bar{k}^*/L^2$: $\eta \sim Da^{-1/2}$. Obviously, a continuum description of the porous medium requires $\eta \gg 1$ or $Da \ll 1$. The Darcy and Kozeny-Carman permeabilities are scaled as

$$k_{\rm D} = \frac{\bar{k}_{\rm D}}{\bar{k}^*} = \frac{1 - \phi}{\phi},\tag{19}$$

$$k_{\rm KC} = \frac{\bar{k}_{\rm KC}}{\bar{k}^*} = \frac{(1-\phi)^3}{10\phi^2},$$
 (20)

 $k_{\rm D}$ being the default used in most of the results below, and $k_{\rm KC}$ only used when the two are compared.

Finally, we collect the dimensionless governing equations below:

$$\frac{\partial \phi}{\partial t} + \frac{\partial (\phi v_s)}{\partial x} = 0, \tag{21}$$

$$\frac{\partial}{\partial x}[\phi v_s + (1 - \phi)v_f] = 0, \tag{22}$$

$$\frac{1-\phi}{k}(v_f - v_s) + \frac{\partial p}{\partial x} = 0, \tag{23}$$

$$\frac{\partial(\phi\sigma_s)}{\partial x} - \frac{\partial p}{\partial x} = 0, \tag{24}$$

$$\frac{\partial(\phi\sigma_s)}{\partial x} - \frac{\partial p}{\partial x} = 0,$$

$$\sigma_s + \frac{\phi_m - \phi_0}{\phi_0} \frac{\phi - \phi_0}{\phi(\phi_m - \phi)} = 0,$$
(24)

where k is the dimensionless permeability of Eq. (19) or (20). The boundary conditions are:

Entry to hydrogel:
$$\sigma_s = -\frac{1+\phi^2}{\phi(1-\phi)^2} \frac{Q-v_s}{\eta}, \qquad (26)$$

Exit of hydrogel:
$$v_s = 0, \quad p = 0.$$
 (27)

3 Model predictions

We will present steady-state Q(P) relationships that exhibit hystereses, and transient simulations of the hystereses as may be realized in an experiment. The steady solutions can be obtained largely analytically following [19]; details are given in Appendix A. The transient simulations are done numerically, adapting a two-dimensional algorithm for flow through hydrogel [36] to the 1D setup here. Either P or Q is varied by small increments, and the other variable evolves in time as a result.

3.1 Hystereses

The interfacial penetration length η is key to interesting dynamics in the Q(P) relationship. Figure 2 depicts the steady-state flux Q as a function of the pressure drop P for a range of η values. Two distinct behaviors can be identified. For smaller η values, e.g., $\eta = 50$, Q initially increases with P, reaches a maximum, and then declines as P increases further. In this regime, there is a single Q value for each P, and no hysteresis exists. At a threshold $\eta \approx 100$, a portion of the Q(P) curve becomes vertical past the maximum. For larger η values, the curve overturns as a breaking wave to produce three Q for an intermediate range of P. Now hysteresis is expected if one varies P in small increments and monitors the reaction of Q. With increasing η , the curve extends farther toward the upper-right of the plot. The hysteresis is delayed to higher ranges of pressure, and the achievable fluxes are also higher.

The non-hysteretic behavior at lower η is straightforward to understand. With increasing P, the solid network is compressed, and the solid fractions ϕ_1 at the upstream interface and ϕ_2 at the downstream interface both increase. This tempers the increase in Q until it reaches a peak. Increasing P further elevates ϕ_2 toward $\phi_m = 1$, with all pores being squeezed shut and the Darcy permeability k_D decreasing toward zero. Thus, our model predicts $Q \to 0$ in the limit of $P \to \infty$. If $\phi_m < 1$, then some pores will persist in the limit of high pressure, and Q will not decline toward zero. This scenario will be considered separately later in this section.

The hysteretic behavior, exemplified by $\eta=150$ in Fig. 2, is more intricate. Transient simulations largely confirm the expectations from the analytical steady solution, with hysteretic jumps when P crosses thresholds while increasing and decreasing (Fig. 3). There is a small discrepancy in that the transient curves seem to "overshoot" the steady solutions slightly near the threshold. This is due to the transient term $\partial \phi/\partial t$ in the continuity equations as well as truncation errors that will diminish with the refinement of time step and mesh size. Examination of the solid velocity shows that the simulation is nearly quasi-static except during the abrupt jumps at the hysteresis.

We can explore the hysteresis from the dynamics of $\phi_1(P)$ in Fig. 3(b), which clearly indicates bistability in the solution for pressure between a lower threshold $P_L = 151.2$ and an upper threshold $P_U = 231.2$ (shown by the vertical dashed lines). There is, of course, a third intermediate solution that is unstable (shown by the grey dashed curve). A slight increase in P would cause the gel layer to compress continually until the solution falls onto the more compressed stable branch with reduced Q, and a slight

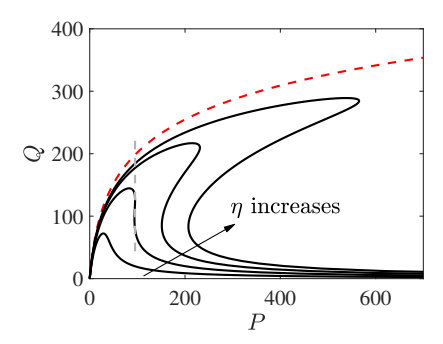


Figure 2: The flux-pressure Q(P) curves at different interfacial penetration $\eta = 50, 100, 150, 200$. The grey dashed line marks the vertical segment of the curve at the threshold $\eta \approx 100$, and the red dashed curve represents the limit of $\eta \to \infty$, at which the stress-free EBC is recovered. The other parameters are $\phi_m = 1$ and $\phi_0 = 0.1$.

decrease in P would cause the solution to jump onto the more expanded stable branch. As P increases from below P_L , the interfacial compression (i.e., the strain e at the interface) remains small and the upstream portion of the gel layer stays "relaxed", until P reaches the upper threshold P_U , when the upstream portion of the gel suddenly becomes "compressed", accompanied by a drop in the fluid velocity. A similar hysteresis occurs when P decreases from above the upper threshold P_U . Note that ϕ_2 changes smoothly across the thresholds, with no hysteresis. Its value is completely determined by the upstream pressure P according to the total force balance $\phi_2\sigma_{s2} + P = 0$, where σ_{s2} is the solid stress at the downstream interface (see Eq. A.6 in Appendix A).

A deeper understanding of the hysteresis can be obtained by noting that the total pressure drop P is expended to overcome two forms of resistance: $P = P_E + P_D$. P_E counters the entry resistance described by the EBC of Eq. (26), with $v_s = 0$ in steady state:

$$P_E = \frac{1 + \phi_1^2}{\eta (1 - \phi_1)^2} Q,\tag{28}$$

whereas P_D balances the Darcy drag in the bulk of the gel layer, and can be computed by integrating the momentum balance of Eq. (23):

$$P_D = Q \int_0^{L_s} \frac{dx}{k_D(\phi)},\tag{29}$$

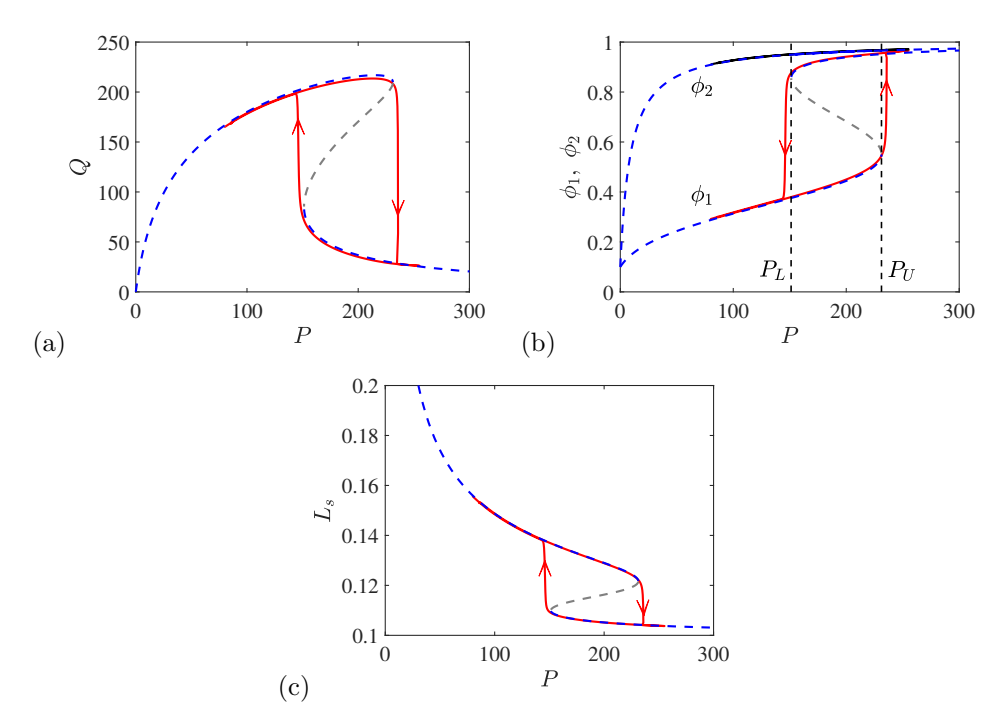


Figure 3: Hysteresis observed at $\eta=150$ by increasing P gradually from P=80 to 255, and then decreasing it back to 80, at a constant rate $dP/dt=\pm2000$. (a) The flux Q as function of the imposed pressure drop P. The red solid lines represent the transient solution, with the arrows marking the direction of the jumps, whereas the blue dashed lines the steady-state solution ($\eta=150$ curve of Fig. 2). (b) The solid fractions ϕ_1 and ϕ_2 at the upstream and downstream gel surface, respectively. The two vertical dashed lines indicate the thresholds P_L and P_U for hysteresis. (c) The thickness of hydrogel layer L_s . The other parameters are $\phi_m=1$ and $\phi_0=0.1$.

where x=0 and $x=L_s$ are the upstream and downstream interfaces of the gel layer, and we have used the continuity equation $(1-\phi)v_f=Q$ in steady state. In keeping with Fig. 3(b), we plot the inverse functions $\phi_1(P_E)$ and $\phi_1(P_D)$ in Fig. 4, together with $\phi_1(P)$. $P_E(\phi_1)$ is monotonic, as can be expected from the interfacial stress balance $P_E=-\phi_1\sigma_{s1}$. Conversely, $P_D(\phi_1)$ has a distinct non-monotonic shape that reflects the fact that at lower P, the flux and Darcy drag increase with P, whereas at high P, compression of the gel causes the flux and Darcy drag to decrease with P. In the limit of large P, $P_D \to 0$ and the P and P_E curves converge. A small interfacial penetration, say $\eta=50$, favors P_E relative to P_D so that the $\phi_1(P)$ curve retains the monotonicity of $\phi_1(P_E)$ (Fig. 4a), and no hysteresis appears. A larger $\eta=150$ tends to reduce P_E and accentuate the role of P_D so as to produce a multi-valued $\phi_1(P)$ curve (Fig. 4b). Now we can understand why the hysteresis occurs only for a sufficiently large interfacial permeability η , which brokers the tradeoff between pressure losses at the interface and in the interior of the gel.

It is only thanks to gel compression that P_E manages to compete with P_D and make the hysteresis possible. In a rigid porous medium, we can estimate the entry pressure drop using a scaling argument, $\bar{P}_E \sim \bar{\mu}\bar{Q}/\bar{r}$, and the bulk pressure drop based on Poiseuille flow, $\bar{P}_D \sim \bar{\mu}\bar{Q}\bar{L}/\bar{r}^2$. Thus, one expects $P_E/P_D = \bar{P}_E/\bar{P}_D \sim \bar{r}/\bar{L} \ll 1$. This inequality indeed holds for small P in both plots of Fig. 4, where the gentle pressure has barely compressed the gel. With increasing P and more severe compression, however, the Darcy flow is suppressed and eventually P_D drops below P_E .

All the discussion so far has assumed a maximum solid fraction $\phi_m=1$. That is to say, as the pressure increases without bound, the fluid pores will eventually be completely closed. In reality, however, strain-hardening of the solid material and the shape of the solid grains may be such that some pores will remain open regardless of the pressure imposed. Having $\phi_m < 1$ allows a second rise of Q with P as $\phi \to \phi_m$, and the possibility of a second kind of hysteresis that occurs when Q is varied continually. This is illustrated in Fig. 5 for $\phi_m = 0.9$.

The left portion of the Q(P) curve resembles that of Fig. 3(a), albeit for a lower $\eta=50$ without the first kind of hysteresis. For the moment, let us imagine increasing P gradually as before. Q increases with P until the peak A, and then declines as the medium continues to compact, till the nadir at D. Afterwards, instead of continually declining toward 0, Q turns up and increases with P without bound, thanks to a minimum level of porosity that persists despite the increasing P. Now if we change the protocol to gradually varying Q, a second type of hysteresis appears, from point A to

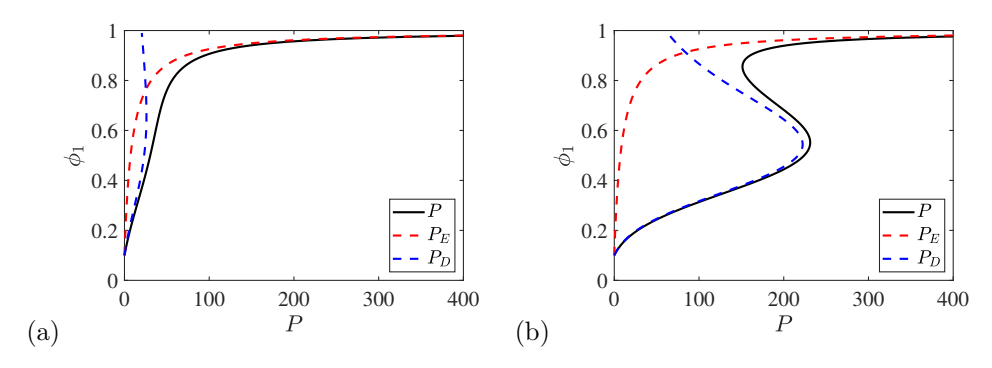


Figure 4: The solid fraction at the interface, ϕ_1 , changes with the total pressure drop P at (a) $\eta=50$ and (b) $\eta=150$. P is divided into the interfacial pressure drop P_E (red dashed line) and the bulk Darcy pressure drop P_D (blue dashed line).

B with increasing Q, and from point D to C with decreasing Q, each accompanied by a sudden jump in P. Of course, each jump corresponds also to a jump in the solid fraction (Fig. 5b), with sudden compaction (A \rightarrow B) or expansion (D \rightarrow C) of the gel layer. One important difference between the two kinds of hystereses is the behavior of ϕ_2 . In the first kind, ϕ_2 varies smoothly with P (Fig. 3b), whereas in the second, ϕ_2 experiences hysteresis with changing Q (Fig. 5b).

In terms of its physical origin, therefore, the second kind of hysteresis is rather straightforward. In comparison, the first kind is more intricate and warrants further analysis. It turns out to hinge on the entry boundary condition (Eq. 26) as well as the bulk permeability (Eq. 19). In what follows, we keep $\phi_m = 1$ and examine each factor in turn.

3.2 Effect of the entry boundary condition

To test the effect of the entry boundary condition (EBC), we replace our EBC (Eq. 26) by the stress-free EBC (Eq. 13). The latter implies zero compression at the upstream surface of the gel: $\phi_1 = \phi_0$. This can be plugged into the flux Q of Eq. (A.4), which, together with ϕ_2 of Eq. (A.7), gives us the red dashed Q(P) curve of Fig. 2 corresponding to the $\eta \to \infty$ limit. It differs from the finite- η curves of Fig. 2 in two obvious ways: Q increases monotonically with P, and $Q \to \infty$ as $P \to \infty$. Both can be easily verified from equations (A.4) and (A.7), and they reflect the fact that $\phi_2 \to 1$ and $Q \propto -\ln(1-\phi_2)$ as $P \to \infty$. Note that the second feature is despite the fact $\phi_m = 1$.

With the stress-free EBC, therefore, no hysteresis exists. This is consistent with our previous observation that the hysteresis stems from a tradeoff between interfacial compression and bulk compression in the gel layer.

3.3 Effect of the bulk permeability

In this test, we replace the Darcy permeability $k_{\rm D}$ (Eq. 19) by the Kozeny-Carman permeability $k_{\rm KC}$ (Eq. 20), while retaining our EBC (Eq. 26). Algebraically, the solution procedure is affected only by replacing Eq. (A.4) with Eq. (A.5). The solution is depicted in Fig. 6 for $\eta = 50,100$ and 200 by the three solid curves.

At each η , Q rises monotonically with increasing P toward a finite asymptotic value. With increasing η , this asymptote increases toward an upper bound, indicated by the

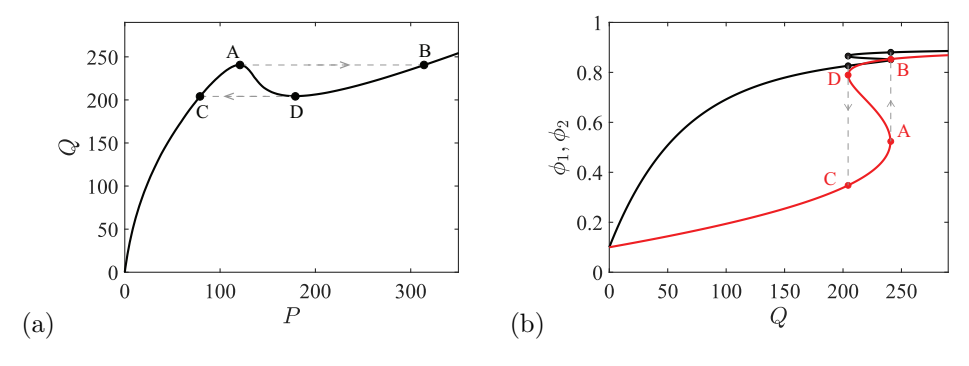


Figure 5: (a) A second type of hysteresis at $\phi_m = 0.9$ and $\eta = 150$, with sudden jumps in P for gradually changing Q, indicated by the grey dashed lines and arrows. (b) The variations of ϕ_1 (red line) and ϕ_2 (black line) with the gradually varying Q. Note the different abscissa from Fig. 3(b).

red dashed curve, which coincides with the solution of Hewitt et al. [19] based on $k_{\rm KC}$ and the stress-free EBC. In our solution, therefore, changing the bulk permeability from $k_{\rm D}$ to $k_{\rm KC}$ has two significant consequences: the first kind of hysteresis disappears, and the asymptotic limit of $Q(P \to \infty)$ changes from zero to a finite value. Both can be understood by analyzing the interplay between the interfacial resistance and the Darcy drag in the bulk.

To rationalize the first kind of hysteresis in Fig. 3, we separated the total pressure P into two parts, P_E and P_D . The same analysis applies here, except that the bulk pressure drop due to Darcy drag, P_D , takes on different forms according to the permeability function k_D or k_{KC} :

$$P_D^{\rm D} = Q \int_0^{L_s} \frac{\phi}{1 - \phi} dx, \quad P_D^{\rm KC} = Q \int_0^{L_s} \frac{10\phi^2}{(1 - \phi)^3} dx.$$
 (30)

The interfacial resistance P_E remains the same as in Eq. (28). The change from $k_{\rm D}$ to $k_{\rm KC}$ has given P_D much more weight relative to P_E . This is because $k_{\rm KC}$ is more sensitive to ϕ ; as the gel is compressed and ϕ rises in the bulk, $k_{\rm KC}(\phi)$ falls more steeply than $k_{\rm D}(\phi)$. As a result, $P_D^{\rm KC}$ rises faster than P_E of Eq. (28). This demands more of P_E to be expended on Darcy drag, and thus gives the bulk resistance more weight relative to the interfacial resistance.

The elevation of P_D relative to P_E explains the two main differences brought on by $k_{\rm KC}$. First, because of the reduced role of P_E , it can no longer compete effectively with P_D (more details in Appendix B). In particular, the gel layer compacts monotonically with P (Fig. B.1), and the first type of hysteresis, seen at higher η in Fig. 2, disappears. A smaller η does raise P_E relative to P_D , but its effect is minor and inadequate. If, however, one modifies the EBC ad hoc to give it a stronger dependence on $(1-\phi)$, this can raise the importance of P_E and restore the hysteresis (see Appendix B for details). Second, the asymptotic behavior at $P \to \infty$ is now dominated by P_D . This behavior has been analyzed by Hewitt et al. [19] before, albeit for their zero-stress EBC. Their analysis applies here because the effect of P_E (determined by the EBC) is insignificant. In particular, as P increases, $\phi_2 \to 1$ and $k_{\rm KC}$ drops sufficiently rapidly to provide enough resistance to counter the higher P. Thus the flux Q tends to a finite constant as $P \to \infty$. In fact, Hewitt et al. [19] showed how this limit is governed in general by the competition between the $k(\phi)$ and $\sigma_s(\phi)$ constitutive equations.

To summarize, both the entry boundary condition and the bulk permeability are

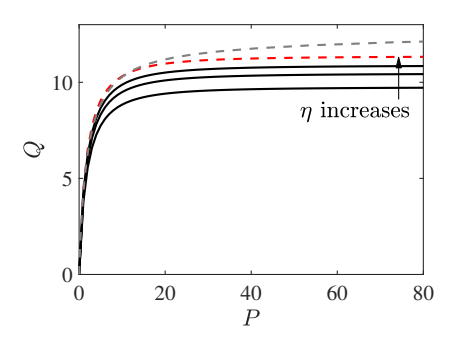


Figure 6: The flux-pressure curve with our entry boundary condition (Eq. 26) and the Kozeny-Carman permeability model (Eq. 20), for $\phi_m = 1$, $\phi_0 = 0.1$ and $\eta = 50, 100, 200$ (the three solid curves). The red dashed curve represents the limit of $\eta \to \infty$. The grey dashed curve shows the effect of strain-hardening, with $\phi_m = 0.9$, $\phi_0 = 0.1$ and $\eta = 200$.

important to the Q(P) curve. The zero-stress EBC ensures Q increasing monotonically with P for either permeability model. Our EBC, on the other hand, introduces an interfacial barrier that allows the interplay between the two opposing effects of increasing P—increasing Darcy flow and compacting the porous medium—and the possibility of a non-monotonic Q(P) curve. The first kind of hysteresis appears if the interfacial resistance plays a prominent role. Changing the Darcy permeability $k_{\rm D}$ to the Kozeny-Carman $k_{\rm KC}$ diminishes that role and suppresses the first kind of hysteresis.

Incidentally, either the zero-stress EBC or the bulk permeability $k_{\rm KC}$ will also eliminate the second kind of hysteresis, because under either condition, Q increases monotonically with P. This is illustrated by the grey dashed curve in Fig. 6 for $\phi_m = 0.9$ and $\eta = 200$. The strain-hardening resists network compaction and yields a higher Q than the solid curve for $\phi_m = 1$ and $\eta = 200$. As ϕ approaches ϕ_m with increasing P, Q increases without bound.

3.4 Relevance to real materials

Can the two kinds of hystereses be observed in the laboratory? The first kind requires three conditions: a bulk permeability that allows the entry pressure P_E to compete with the bulk pressure P_D , a sufficiently large η value, and a sufficiently high range for the pressure P. Of the two permeabilities tested, k_D allows the hysteresis but k_{KC} does not, because k_{KC} declines too rapidly with rising solid fraction ϕ . Although other forms of bulk permeability are possible [52], in general a high porosity favors k_D over k_{KC} [39]. Hydrogels can have an initial solid fraction ϕ_0 of a few percent or lower [43, 45], and their high porosity should be conducive to the first kind of hysteresis.

The dimensionless $\eta = 4.5\bar{L}/\bar{r}$ represents the number of pores within the gel thickness. The hysteresis requires $\eta \geq 100$, or $\bar{L}/\bar{r} \geq 22.2$, an easily achieved goal in laboratory experiments. Take a pore size of $\bar{r} = 50$ microns [44,53,54], this requirement amounts to a gel thickness greater than 1.1 mm.

Finally, our dimensionless pressure P has been scaled by the Young's modulus \bar{E} of the solid network, defined in Eq. (11). There have been numerous reports of Young's modulus for hydrogels, measured using macroscopic or AFM indentation and micropipette aspiration, among other methods [55]. \bar{E} is sensitive to the solid content in the gel and the degree of crosslinking, ranging from $\bar{E} \sim 100$ Pa for the softer polyacrylamide and poly(ethylene glycol) hydrogels [56, 57] to a few kPa for collagen and ECM gels [58]. Taking $\bar{E}=500$ Pa as an example, the first kind of hysteresis can be observed for $P\sim 200$ or a dimensional pressure $\bar{P}\sim 100$ kPa, within the range of prior compression experiments [23]. Of course, thicker gel layers, with a larger η , will require a higher P.

The second kind of hysteresis, illustrated in Fig. 5, requires a non-monotonic Q(P) curve, strain-hardening with a solid fraction $\phi_m < 1$ at maximum compaction, and a sufficiently high pressure to achieve maximum compaction. These are essentially the same requirements as for the first kind of hysteresis, plus an additional one on strain-hardening. Strain-hardening is a well-known characteristic of soft tissues and biological gels [59], and to a lesser extent also of synthetic gels [48]. So far, the quantification of strain-hardening is mostly through shear and uniaxial elongation or compression [46,47]. We have found no report of 1D compression of hydrogel layers. Typically, uniaxial compression exhibits a maximum strain at which the stress diverges [47,48]. Assuming the kinematics of 1D compression, we can infer maximum solid fractions $\phi_m \sim 0.6$ from the uniaxial-compression data for double-network hydrogels [47]. Based on the limited knowledge available, we expect the strongest strain-hardening, with the lowest ϕ_m , for biological tissues or "reinforced hydrogels", e.g., via a second network. Such materials can exhibit strong resistance to compression, thanks to microstructures that

may maintain a finite porosity under high pressure.

It is interesting that previous experiments by Li et al. [10,16] have already reported non-monotonic dependence of Q on P owing to gel compression in a confined channel. But their geometry is multi-dimensional, and compression from the side walls may have contributed to the compaction of the gel. In addition, McGuire et al. [15] have observed a bell-shaped Q(P) curve in intratumoral infusion, and attributed it to the tissue being compressed by the interstitial flow in a spherically symmetric geometry. In both cases, the non-monotonic Q(P) can be likened to our model prediction for a lower η (Fig. 2). Unidirectional 1D compression has been tested in deformable porous media made of packed beds of soft spheres or foam [19,23]. Those experiments have documented hystereses in the Q(P) curve when P is varied, but ascribed them to factors such as particle rearrangement or wall friction. They are probably unrelated to our first kind of hysteresis. In fact, such macroscopic porous media have high solid fraction ($\phi_0 \sim 0.6$) and large sample sizes, both factors disfavoring the realization of the hysteresis predicted here. The high ϕ_0 means that the material probably follows the Kozeny-Carman permeability rather than the Darcy permeability [19]. A large sample thickness implies large η values, which would in turn raise the pressure P required to access the hysteresis (Fig. 2). For example, Hewitt et al. [19] had pore radius $\bar{r} = 0.19$ mm and gel thickness $\bar{L} = 11.4$ cm, and thus $\eta = 2700$. Lutz et al. [23] had $\bar{r} = 0.025$ mm, $\bar{L} = 8$ cm and $\eta = 14400$. Both η values are much higher than those tested here in our study, and the hysteresis would require much higher pressure than those employed in their experiments.

Based on the discussion above, one can probe the first kind of hysteresis by using high-porosity, soft gels at a moderate gel thickness. The second kind would further require strong strain-hardening under compression, as typically found in biological tissues, biopolymer-based or double-network hydrogels.

4 Conclusion

Using a poroelastic model, we predict two types of hysteresis when a hydrogel layer is compressed by a uniform flow normal to the layer. The first type happens when the pressure drop over the hydrogel layer is gradually increased or decreased; the flux may undergo sudden jumps at different thresholds of pressure and form a hysteresis loop. The second type occurs when the flux is controlled, with the pressure jumping discontinuously.

The physics underlying these hystereses can be understood from how the flow compresses the porous medium to reduce the permeability and produce a non-monotonic relationship between the flux Q and pressure drop P. For the first kind of hysteresis, the mechanism can be traced further to the competition between interfacial and bulk compression. The former determines the entrance pressure drop P_E across the upstream interface, whereas the latter affects the pressure drop P_D through the bulk of the gel to overcome the Darcy drag. The two add up to the total pressure drop P. This type of hysteresis can be suppressed by a bulk permeability that drops too sharply with diminishing porosity as the pores are squeezed by increasing pressure. This makes P_D dominant over P_E and obviates their competition. If we then modify the form of the interfacial permeability to strengthen P_E , the hysteresis can be restored.

The second kind of hysteresis hinges on strain-hardening of the solid network in the hydrogel such that some pores stay open regardless of how high P becomes. This ensures that after a decline of Q with P owing to compaction of the gel layer, Q will eventually rise again at higher P. Thus, the second type of hysteresis occurs when Q is controlled and varied gradually.

To seek the hystereses predicted here in a laboratory experiment, one should choose

material properties and geometries conducive to each kind. The first kind of hysteresis is facilitated by high-porosity, low-modulus hydrogels of moderate thickness; these factors favor interfacial compression over bulk compression. The second kind hinges on strain-hardening against compression, and requires strong gels that can maintain porosity under high pressure. As many engineering and biomedical processes involve compression of soft porous materials [19,21,25], the presence of hysteresis will have an impact on such applications. For example, sudden changes in flow rate during injection into biological tissues [15] or geological formations [60] may be undesirable. But hysteresis can also be exploited in designing smart sensors and actuators [61].

Acknowledgements: J.J.F. acknowledges financial support by Natural Sciences and Engineering Research Council of Canada (Discovery Grant No. 2019-04162, 2024-03982, Alliance International Grant No. 586462-23). P.Y. acknowledges the financial support by National Science Foundation (Grants DMS-2012480, DMS-2309732). We thank Neil Balmforth, Arun Ramchandran and Boris Stoeber for helpful discussions.

Appendix A Steady-state solution

Here we illustrate the algebraic procedure for obtaining the steady-state Q(P) curve for our model, following a similar procedure in Hewitt *et al.* [19]. This is accomplished in two steps. First, integrating the continuity and momentum equations, we derive an algebraic formula linking Q to P and the solid fraction ϕ_1 at the upstream surface of the gel layer. Second, from the EBC we derive another algebraic formula linking Q to ϕ_1 . Between the two formulae, Q(P) is obtained.

In the steady state, the Darcy drag compresses the solid skeleton to establish a $\phi(x)$ profile. From the governing equations of poroelasticity, we can relate the steady flux Q to this $\phi(x)$ profile. This relationship is general, and can be specialized to the different permeability functions $k_{\rm D}$ and $k_{\rm KC}$. We start from an overall solid-volume conservation equation:

$$\int_0^{L_s} \phi(x) \, dx = \phi_0,\tag{A.1}$$

where x = 0 is the upstream interface of the gel layer and $x = L_s$ the downstream interface. Following Hewitt *et al.* [19], we use the continuity and momentum equations to relate the flux to the solid stress:

$$Q = -k \frac{\partial (\phi \sigma_s)}{\partial x} = -k \frac{\partial (\phi \sigma_s)}{\partial \phi} \frac{\partial \phi}{\partial x} = -k(\phi \sigma_s' + \sigma_s) \frac{\partial \phi}{\partial x}, \tag{A.2}$$

where the bulk permeability k can be $k_{\rm D}$ or $k_{\rm KC}$. Now Eq. (A.1) can be transformed into $\int_{\phi_1}^{\phi_2} -\phi k(\phi \sigma_s' + \sigma_s)/Q \, d\phi = \phi_0$, with $\phi_1 = \phi(0)$, $\phi_2 = \phi(L_s)$. Thus

$$Q = \int_{\phi_1}^{\phi_2} \frac{\phi k(\phi \sigma_s' + \sigma_s)}{\phi_0} d\phi. \tag{A.3}$$

Again, this holds in steady state for all EBCs and all $k(\phi)$ forms. Using the constitutive equation for σ_s (Eq. 25) and the Darcy permeability $k_{\rm D}$ (Eq. 19), we integrate analytically to obtain

$$Q = \frac{(\phi_m - \phi_0)^2}{\phi_0^2} \left[\frac{(1 - \phi_m)(\phi_2 - \phi_1)}{(\phi_1 - \phi_m)(\phi_2 - \phi_m)} + \ln \frac{\phi_m - \phi_1}{\phi_m - \phi_2} \right]$$

$$\xrightarrow{\phi_m \to 1} \frac{(1 - \phi_0)^2}{\phi_0^2} \ln \frac{1 - \phi_1}{1 - \phi_2}.$$
(A.4)

For later reference, we can carry out the integration using the Kozeny-Carman permeability $k_{\rm KC}$ (Eq. 20) to get

$$Q = \frac{(\phi_m - \phi_0)^2}{10\phi_0^2} \left(\phi_1 - \phi_2 + \phi_m \ln \frac{\phi_2}{\phi_1}\right)$$

$$\xrightarrow{\phi_m \to 1} \frac{(1 - \phi_0)^2}{10\phi_0^2} \left(\phi_1 - \phi_2 + \ln \phi_2 - \ln \phi_1\right). \tag{A.5}$$

The solid fraction ϕ_2 at the downstream surface of the hydrogel is determined by the overall force balance for the whole layer:

$$-\phi_2 \sigma_{s2} = P, \tag{A.6}$$

where P is the pressure in the upstream clear fluid and the pressure downstream of the gel layer is set to zero. Since the solid stress σ_{s2} is related to ϕ_2 via the constitutive relation (Eq. 25), ϕ_2 can be solved from Eq. (A.6) as

$$\phi_2 = \phi_0 \xrightarrow{\phi_m - \phi_0 + P\phi_m} \xrightarrow{\phi_m \to 1} \phi_0 \xrightarrow{1 - \phi_0 + P} (A.7)$$

Note that as $P \to \infty$, the solid fraction at the downstream edge of the compressed gel $\phi_2 \to \phi_m$, as expected. Using $\phi_2(P)$, we can express Q in terms of P and the solid fractions ϕ_1 , the latter depending on the EBC.

Our EBC of Eq. (26) relates Q to ϕ_1 . In steady state, this becomes

$$Q = -\eta \frac{\phi_1 (1 - \phi_1)^2}{(1 + \phi_1^2)} \sigma_s(\phi_1). \tag{A.8}$$

Plugging in the solid stress σ_s of Eq. (25) evaluated at $\phi = \phi_1$, we obtain

$$Q = \eta \frac{(1 - \phi_1)^2}{(1 + \phi_1^2)} \frac{\phi_m - \phi_0}{\phi_0} \frac{\phi_1 - \phi_0}{\phi_m - \phi_1} \xrightarrow{\phi_m \to 1} \eta \frac{(1 - \phi_0)}{\phi_0} \frac{(1 - \phi_1)(\phi_1 - \phi_0)}{(1 + \phi_1^2)}, \tag{A.9}$$

which is a function of ϕ_1 with η as a parameter. Eliminating ϕ_1 and ϕ_2 from equations (A.4), (A.7) and (A.9), we obtain Q(P) with η as a parameter. Algebraic complexity precludes an analytical expression and numerical calculations are used to generate the data in Fig. 2. A similar procedure works for the zero-compression EBC of Hewitt et al. [19] (Eq. 13) and the Kozeny-Carman permeability model (Eq. 20).

Appendix B Further analysis of the bulk permeability

As noted in section 3.3 of the main text, changing the bulk permeability model from $k_{\rm D}$ to $k_{\rm KC}$ (Eqs. 19, 20) suppresses the first kind of hysteresis, and changes the large-pressure limit of the flux from zero to a finite value. Both can be traced to the fact that $k_{\rm KC}$ elevates the importance of the bulk pressure drop P_D , due to the Darcy drag, relative to the interfacial pressure drop P_E , due to the entrance boundary condition.

To demonstrate the dominance of P_D over P_E with bulk permeability $k_{\rm KC}$, we plot their relationship to the interfacial solid fraction ϕ_1 in Fig. B.1. Physically it might be more intuitive to think of P, P_E and P_D as functions of ϕ_1 , but ϕ_1 is plotted as the dependent variable to facilitate comparisons with figures 3 and 4 in the main text. A key difference from Fig. 4 is that now P_D dominates P_E over the entire range of pressures. Consequently, the interfacial compression becomes much milder than with the Darcy

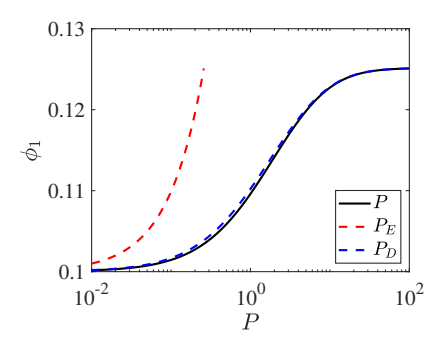


Figure B.1: The solid fraction ϕ_1 as functions of the pressure P and its two components P_E and P_D at interfacial penetration $\eta = 50$. The other parameters are $\phi_m = 1$ and $\phi_0 = 0.1$. Relative to the bulk permeability k_D , k_{KC} elevates the importance of P_D so that it dominates P_E . At larger η values, P_E will be even smaller according to Eq. (28).

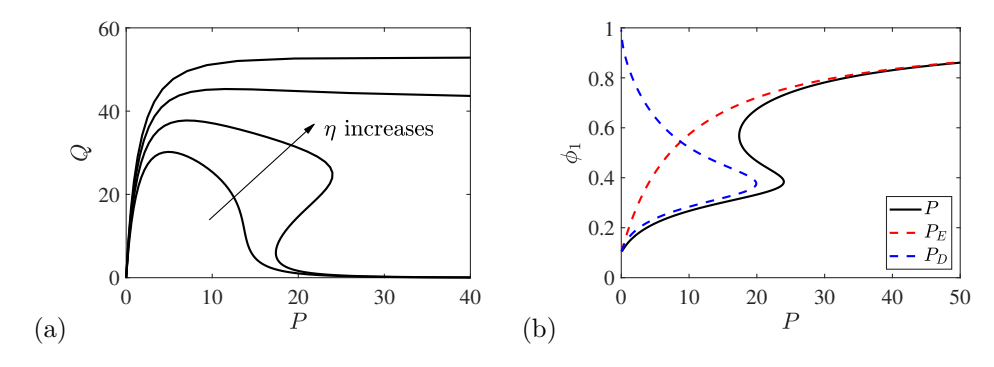


Figure B.2: An artificially modified EBC restores the first kind of hysteresis with the Kozeny-Carman permeability model (Eq. 20). (a) The flux-pressure curve with our high-order EBC (Eq. B.1) for $\eta = 100$, 125, 150, 175. (b) The interfacial solid fraction ϕ_1 as functions of the total pressure P and its components P_E and P_D at $\eta = 125$.

permeability k_D . These differences obviate the competition between the two pressure drops and eliminate the hysteresis.

To provide additional support to the above argument, we elevate *ad hoc* the interfacial resistance P_E and demonstrate that this can restore its competition with P_D and reinstate the hysteresis. This can be accomplished by raising the power of the porosity in the EBC (Eq. 26) from 2 to 6, so as to produce an interfacial pressure drop

$$P_E = \frac{Q}{\eta} \frac{\phi_1^2 + 1}{(1 - \phi_1)^6} \tag{B.1}$$

with a stronger dependence on $1-\phi$ than P_D^{KC} of Eq. (30). For this new EBC, Fig. B.2(a) presents a series of Q(P) curves for increasing values of η . For smaller η , such as 100 and 125, the flux Q increases initially before declining as $P \to \infty$. This is owing to the fact that P_D is now dominated by P_E in that limit (Fig. B.2b). Importantly, a hysteresis of the first kind reappears for $\eta=125$. Even greater values of η , however, are able to weaken P_E sufficiently to suppress the hysteresis again. For example, at $\eta=175$, $\phi_1 \to 0.244$ as $P \to \infty$, only moderately above $\phi_0=0.1$ and much below the limit of Fig. B.2(b). Such a mild interfacial compression is again unable to compete with P_D . In this case, Q tends to a finite non-zero asymptote as in Fig. 6.

References

- [1] O. Okay, General properties of hydrogels, in: G. Gerlach, K. F. Arndt (Eds.), Hydrogel Sensors and Actuators, Springer, 2009, pp. 1–14.
- [2] Q. Liang, X. Xia, X. Sun, D. Yu, X. Huang, G. Han, S. M. Mugo, W. Chen, Q. Zhang, Highly stretchable hydrogels as wearable and implantable sensors for recording physiological and brain neural signals, Adv. Sci. 9 (2022) 2201059.
- [3] R. Barbucci, V. Spera, E. Armenia, V. Quagliariello, Microarchitecture of water confined in hydrogels, Hydrogels: Design, Synthesis and Application in Drug Delivery and Regenerative Medicine (2018) 1.
- [4] M. Tunesi, L. Izzo, I. Raimondi, D. Albani, C. Giordano, A miniaturized hydrogel-based in vitro model for dynamic culturing of human cells overexpressing beta-amyloid precursor protein, J. Tissue Eng. 11 (2020) 2041731420945633.
- [5] E. L. Doherty, W. Y. Aw, A. J. Hickey, W. J. Polacheck, Microfluidic and organ-ona-chip approaches to investigate cellular and microenvironmental contributions to cardiovascular function and pathology, Front. Bioeng. Biotechnol. 9 (2021) 624435.
- [6] D. J. Beebe, J. S. Moore, J. M. Bauer, Q. Yu, R. H. Liu, C. Devadoss, B.-H. Jo, Functional hydrogel structures for autonomous flow control inside microfluidic channels, Nature 404 (6778) (2000) 588–590.
- [7] J. P. Gong, W. Hong, Mechanics and physics of hydrogels, Soft Matter 8 (2012) 8006–8007.
- [8] M. Bacca, R. M. McMeeking, A viscoelastic constitutive law for hydrogels, Meccanica 52 (2017) 3345–3355.
- [9] J.-F. Louf, S. S. Datta, Poroelastic shape relaxation of hydrogel particles, Soft Matter 17 (2021) 3840–3847.
- [10] Y. Li, O. S. Sariyer, A. Ramachandran, S. Panyukov, M. Rubinstein, E. Kumacheva, Universal behavior of hydrogels confined to narrow capillaries, Sci. Rep. 5 (2015) 17017.
- [11] C. W. MacMinn, E. R. Dufresne, J. S. Wettlaufer, Large deformations of a soft porous material, Phys. Rev. Appl. 5 (2016) 044020.
- [12] Y. Gao, H. J. Cho, Quantifying the trade-off between stiffness and permeability in hydrogels, Soft Matter 18 (2022) 7735–7740.
- [13] K. H. Parker, R. V. Mehta, C. G. Caro, Steady flow in porous, elastically deformable materials, J. Appl. Mech. 54 (1987) 794–800.
- [14] X.-Y. Zhang, J. Luck, M. W. Dewhirst, F. Yuan, Interstitial hydraulic conductivity in a fibrosarcoma, Am. J. Physiol. Heart Circ. Physiol. 279 (6) (2000) H2726–H2734.
- [15] S. McGuire, D. Zaharoff, F. Yuan, Nonlinear dependence of hydraulic conductivity on tissue deformation during intratumoral infusion, Ann. Biomed. Eng. 34 (2006) 1173–1181.
- [16] Y. Li, E. Kumacheva, A. Ramachandran, The motion of a microgel in an axisymmetric constriction with a tapered entrance, Soft Matter 9 (2013) 10391–10403.

- [17] Y. Li, Y. Li, E. Prince, J. I. Weitz, S. Panyukov, A. Ramachandran, M. Rubinstein, E. Kumacheva, Fibrous hydrogels under biaxial confinement, Nat. Comm. 13 (2022) 3264.
- [18] D. R. Hewitt, J. A. Neufeld, N. J. Balmforth, Shallow, gravity-driven flow in a poro-elastic layer, J. Fluid Mech. 778 (2015) 335–360.
- [19] D. R. Hewitt, J. S. Nijjer, M. G. Worster, J. A. Neufeld, Flow-induced compaction of a deformable porous medium, Phys. Rev. E 93 (2016) 023116.
- [20] C. W. MacMinn, E. R. Dufresne, J. S. Wettlaufer, Fluid-driven deformation of a soft granular material, Phys. Rev. X 5 (2015) 011020.
- [21] D. T. Paterson, T. S. Eaves, D. R. Hewitt, N. J. Balmforth, D. M. Martinez, Flow-driven compaction of a fibrous porous medium, Phys. Rev. Fluids 4 (2019) 074306.
- [22] D. T. Paterson, T. S. Eaves, D. R. Hewitt, N. J. Balmforth, D. M. Martinez, One-dimensional compression of a saturated elastoviscoplastic medium, Phys. Rev. Fluids 7 (2022) 054303.
- [23] T. Lutz, L. Wilen, J. Wettlaufer, A method for measuring fluid pressure and solid deformation profiles in uniaxial porous media flows, Rev. Sci. Instrum. 92 (2021) 025101.
- [24] Z. Xu, J. Zhang, Y.-N. Young, P. Yue, J. J. Feng, A comparison of four boundary conditions for the fluid-hydrogel interface, Phys. Rev. Fluids 7 (2022) 093301.
- [25] Z. Xu, P. Yue, J. J. Feng, Poroelastic modeling reveals the cooperation between two mechanisms for albuminuria, J. R. Soc. Interface 20 (2023) 20220634.
- [26] S. Haber, R. Mauri, Boundary conditions for Darcy's flow through porous media, Int. J. Multiphase Flow 9 (1983) 561–574.
- [27] J. Koplik, H. Levine, A. Zee, Viscosity renormalization in the Brinkman equation, Phys. Fluids 26 (1983) 2864–2870.
- [28] J. H. Masliyah, G. Neale, K. Malysa, T. G. M. Van De Ven, Creeping flow over a composite sphere: Solid core with porous shell, Chem. Eng. Sci. 42 (1987) 245–253.
- [29] L. Preziosi, D. D. Joseph, G. S. Beavers, Infiltration of initially dry, deformable porous media, Int. J. Multiphase Flow 22 (1996) 1205–1222.
- [30] U. Lācis, S. Bagheri, A framework for computing effective boundary conditions at the interface between fluid and a porous medium, J. Fluid Mech. 812 (2017) 866–889.
- [31] T. Carraro, C. Goll, A. Marciniak-Czochra, A. Mikelic, Pressure jump interface law for the Stokes-Darcy coupling: confirmation by direct numerical simulations, J. Fluid Mech. 732 (2013) 510–536.
- [32] T. Carraro, C. Goll, A. Marciniak-Czochra, A. Mikelić, Effective interface conditions for the forced infiltration of a viscous fluid into a porous medium using homogenization, Comput. Methods Appl. Mech. Eng. 292 (2015) 195–220.
- [33] U. Lācis, Y. Sudhakar, S. Pasche, S. Bagheri, Transfer of mass and momentum at rough and porous surfaces, J. Fluid Mech. 884 (2020) A21.

- [34] Y.-N. Young, Y. Mori, M. J. Miksis, Slightly deformable Darcy drop in linear flows, Phys. Rev. Fluids 4 (2019) 063601.
- [35] J. J. Feng, Y.-N. Young, Boundary conditions at a gel-fluid interface, Phys. Rev. Fluids 5 (2020) 124304.
- [36] L. Li, J. Zhang, Z. Xu, Y.-N. Young, J. J. Feng, P. Yue, An arbitrary Lagrangian-Eulerian method for simulating interfacial dynamics between a hydrogel and a fluid, J. Comput. Phys. 451 (2022) 110851.
- [37] M. Minale, Momentum transfer within a porous medium. II. Stress boundary condition, Phys. Fluids 26 (2014) 123102.
- [38] O. Coussy, Poromechanics, John Wiley & Sons, 2004.
- [39] F. A. L. Dullien, Chapter 3: Single-phase transport phenomena in porous media, in: Porous Media: Fluid Transport and Pore Structure, 2nd Edition, Academic Press, San Diego, 1992, pp. 237–317.
- [40] R. E. Caflisch, J. Rubinstein, Chapter 6: Flow in porous media, in: Lectures on the mathematical theory of multi-phase flow, New York University, 1986, pp. 64–76.
- [41] H. C. Brinkman, A calculation of the viscous force exerted by a flowing fluid on a dense swarm of particles, Appl. Sci. Res. A1 (1947) 27–34.
- [42] T. S. Lundgren, Slow flow through stationary random beds and suspensions of spheres, J. Fluid Mech. 51 (1972) 273–299.
- [43] N. Annabi, J. W. Nichol, X. Zhong, C. Ji, S. Koshy, A. Khademhosseini, F. Dehghani, Controlling the porosity and microarchitecture of hydrogels for tissue engineering, Tissue Eng. B 16 (2010) 371–383.
- [44] A. Salerno, R. Borzacchiello, P. A. Netti, Pore structure and swelling behavior of porous hydrogels prepared via a thermal reverse-casting technique, J. Appl. Polym. Sci. 122 (2011) 3651–3660.
- [45] S. Kovačič, M. S. Silverstein, Superabsorbent, high porosity, PAMPS-based hydrogels through emulsion templating, Macromol. Rapid Commun. 37 (2016) 1814–1819.
- [46] F. Furlani, A. Marfoglia, E. Marsich, I. Donati, P. Sacco, Strain hardening in highly acetylated chitosan gels, Biomacromol. 22 (2021) 2902–2909.
- [47] J. P. Gong, Y. Katsuyama, T. Kurokawa, Y. Osada, Double-network hydrogels with extremely high mechanical strength, Adv. Mater. 15 (14) (2003) 1155–1158.
- [48] Y. Cui, M. Tan, A. Zhu, M. Guo, Strain hardening and highly resilient hydrogels crosslinked by chain-extended reactive pseudo-polyrotaxane, RSC Adv. 4 (2014) 56791–56797.
- [49] K. N. Nordstrom, E. Verneuil, W. G. Ellenbroek, T. C. Lubensky, J. P. Gollub, D. J. Durian, Centrifugal compression of soft particle packings: Theory and experiment, Phys. Rev. E 82 (2010) 041403.
- [50] Z. Xu, P. Yue, J. J. Feng, A theory of hydrogel mechanics that couples swelling and external flow, Soft Matter 20 (2024) 5389–5406.

- [51] Z. Xu, P. Yue, J. J. Feng, Estimating the interfacial permeability for flow into a poroelastic medium, Soft Matter (2024) (published online); DOI: 10.1039/D4SM00476K.
- [52] R. Schulz, N. Ray, S. Zech, A. Rupp, P. Knabner, Beyond Kozeny-Carman: Predicting the permeability in porous media, Transp. Porous Med. 130 (2019) 487–512.
- [53] Y.-C. Chiu, M.-H. Cheng, H. Engel, S.-W. Kao, J. C. Larson, S. Gupta, E. M. Brey, The role of pore size on vascularization and tissue remodeling in PEG hydrogels, Biomaterials 32 (2011) 6045–6051.
- [54] S. Sornkamnerd, M. K. Okajima, T. Kaneko, Tough and porous hydrogels prepared by simple lyophilization of LC gels, ACS Omega 2 (8) (2017) 5304–5314.
- [55] D. Lee, H. Zhang, S. Ryu, Elastic modulus measurement of hydrogels, in: M. I. H. Mondal (Ed.), Cellulose-Based Superabsorbent Hydrogels, Springer International Publishing, Cham, 2018, pp. 1–21.
- [56] K. M. Schultz, K. A. Kyburz, K. S. Anseth, Measuring dynamic cellmaterial interactions and remodeling during 3d human mesenchymal stem cell migration in hydrogels, Proc. Natl. Acad. Sci. U.S.A. 112 (29) (2015) E3757–E3764.
- [57] A. Gandin, Y. Murugesan, V. Torresan, L. Ulliana, A. Citron, P. Contessotto, G. Battilana, T. Panciera, M. Ventre, A. P. Netti, L. Nicola, S. Piccolo, G. Brusatin, Simple yet effective methods to probe hydrogel stiffness for mechanobiology, Sci. Rep. 11 (2021) 22668.
- [58] M. Kobayashi, J. Kadota, Y. Hashimoto, T. Fujisato, N. Nakamura, T. Kimura, A. Kishida, Elastic modulus of ecm hydrogels derived from decellularized tissue affects capillary network formation in endothelial cells, Int. J. Mol. Sci. 21 (17).
- [59] C. Storm, J. Pastore, F. C. MacKintosh, T. C. Lubensky, P. A. Janmey, Nonlinear elasticity in biological gels, Nature 435 (2005) 191–194.
- [60] L. Jin, A hydromechanical-stochastic approach to modeling fluid-induced seismicity in arbitrarily fractured poroelastic media: Effects of fractures and coupling, Tectonophysics 826 (2022) 229249.
- [61] X. Shan, H. Song, H. Cao, L. Zhang, X. Zhao, J. Fan, A dynamic hysteresis model and nonlinear control system for a structure-integrated piezoelectric sensoractuator, Sensors 21 (2021) 269.